

DOI: 10.1002/chem.201301498

Mesoporous Core–Shell Fenton Nanocatalyst: A Mild, Operationally Simple Approach to the Synthesis of Adipic Acid

Astam K. Patra, Arghya Dutta, and Asim Bhaumik*^[a]

Abstract: Mesoporous nanoparticles composed of γ - Al_2O_3 cores and α - Fe_2O_3 shells were synthesized in aqueous medium. The surface charge of γ - Al_2O_3 helps to form the core–shell nanocrystals. The core–shell structure and formation mechanism have been investigated by wide-angle XRD, energy-dispersive X-ray spectroscopy, and elemental mapping by ultrahigh-resolution (UHR) TEM and X-ray photoelectron spectroscopy. The N_2 adsorption–desorption isotherm of this core–shell materials, which is of type IV, is characteristic of a mesoporous material having a BET surface area of $385 \text{ m}^2 \text{ g}^{-1}$ and an average pore

size of about 3.2 nm. The SEM images revealed that the mesoporosity in this core–shell material is due to self-aggregation of tiny spherical nanocrystals with sizes of about 15–20 nm. Diffuse-reflectance UV/Vis spectra, elemental mapping by UHRTEM, and wide-angle XRD patterns indicate that the materials are composed of aluminum oxide cores and iron oxide shells. These $\text{Al}_2\text{O}_3@ \text{Fe}_2\text{O}_3$ core–shell nanoparticles

Keywords: core–shell structures • heterogeneous catalysis • mesoporous materials • nanoparticles • oxidation

act as a heterogeneous Fenton nanocatalyst in the presence of hydrogen peroxide, and show high catalytic efficiency for the one-pot conversion of cyclohexanone to adipic acid in water. The heterogeneous nature of the catalyst was confirmed by a hot filtration test and analysis of the reaction mixture by atomic absorption spectroscopy. The kinetics of the reaction was monitored by gas chromatography and ^1H NMR spectroscopy. The new core–shell catalyst remained in a separate solid phase, which could easily be removed from the reaction mixture by simple filtration and the catalyst reused efficiently.

Introduction

The development of green and sustainable strategies for efficient synthesis of fine and bulk chemicals is one of the most fascinating areas of research today.^[1] In the twenty-first century, considerable efforts have been devoted to the preparation of core–shell nanoparticles to improve their properties in catalysis,^[2] separation,^[3] sensors,^[4] biomedical imaging,^[5] electron imaging,^[3b,6] gene delivery,^[7] diagnosis, and therapy^[8] due to their tunable properties and tunable particle sizes through appropriate choice of the core and shell structures in a material. Depending on the choice of the two components, the chemical and physical properties can be varied.^[9] Bimetallic transition metal oxide core–shell nanoparticles have potential uses in catalysis and magnetic and optical applications that are quite distinct from those of their monometallic counterparts.^[1a,10] These core–shell nanoparticles can be specifically designed for utilization as new classes of multifunctional materials.^[5] Generally, the synthe-

sis of porous Fe_2O_3 by the soft-templating method is not convenient, and the resulting materials have low surface areas and poor crystallinity. Recently, we developed a highly efficient method for preparation of γ - Al_2O_3 nanoparticles by using a hydrothermal method and sodium salicylate as template.^[11] Herein, use of these alumina nanoparticles as the core of the nanoparticle helps to form the core–shell structure. These γ - Al_2O_3 nanoparticles were encapsulated by a thin shell of α - Fe_2O_3 , and the resulting material showed high surface area due to self-aggregation of the tiny nanocrystals. These core–shell nanoparticles act as a Fenton catalyst in the presence of H_2O_2 as oxidant and show high catalytic activity for conversion of cyclohexanone to adipic acid in a one-step reaction.

Adipic acid is one of the most important dicarboxylic acids industrially and it has been widely used in the manufacture of polymers for carpet fibers, furniture, tire reinforcement, auto parts, clothing, and so forth.^[12] Most industrial processes for the production of adipic acid involve nitric acid oxidation of cyclohexanol or cyclohexanol–cyclohexanone mixtures.^[13] However, in this process, production of nitrous oxide (N_2O) as an unavoidable chemical waste contributes significantly to global warming. Hence, a green synthetic route for the production of adipic acid is highly desirable. In 1998 adipic acid was produced by direct oxidation of cyclohexenes by using hydrogen peroxide as oxidant and sodium tungstate as catalyst.^[12] To date most of the known reactions have involved tungsten-based catalysts^[14] and hy-

[a] A. K. Patra, A. Dutta, Prof. Dr. A. Bhaumik
Department of Materials Science
Indian Association for the Cultivation of Science
2A and 2B Raja S. C. Mullick Road
Jadavpur, Kolkata 700032 (India)
E-mail: msab@iacs.res.in
Homepage: <http://www.iacs.res.in/matssc/msab/>

Supporting information for this article is available on the WWW under <http://dx.doi.org/10.1002/chem.201301498>.

drogen peroxide or other peroxides as oxidants.^[15] In 2011, adipic acid was also synthesized by selective hydrogenation of *trans,trans*-muconic acid.^[16] However, the cost involved in the synthesis of the catalysts and the catalytic reactions are too high for these catalytic routes to be industrially attractive. In a homogeneous system, cyclohexanone could be converted to adipic acid with molecular oxygen as an oxidant, but in most cases organic solvents, and sometimes high-pressure reactors, are needed to make the process feasible. Besides, it is always desirable to have a heterogeneous catalyst for easy separation of the product from the reaction medium. Microporous FeAlPO-31 has been utilized as heterogeneous catalyst for liquid-phase oxidation of cyclohexanone to adipic acid in the presence of air.^[17] In this context, recently we developed a porous hybrid tin(IV) phosphonate as a heterogeneous catalyst that produces adipic acid from cyclohexanone in the presence of air.^[18] Functionalized microporous and mesoporous materials bearing active metals have long been known as good heterogeneous catalysts for various ecologically friendly catalytic reactions. We have now designed mesoporous core-shell nanoparticles which act as a heterogeneous Fenton catalyst in the presence of H₂O₂ and show high catalytic activity for the one-pot conversion of cyclohexanone to adipic acid in water. The heterogeneous catalyst allows easy separation from the reaction mixture and its recycling. Furthermore, aqueous H₂O₂ is an ideal clean oxidant for the oxidation reaction and thus industrially desirable. In the oxidation reaction, H₂O₂ is converted to water, which makes the reaction a green-chemical procedure.

Herein, we report a new synthetic strategy for the preparation of highly stable mesoporous Al₂O₃@Fe₂O₃ core-shell nanoparticles. The surface charge of γ -Al₂O₃ helps to form the core-shell nanostructure. The core-shell structure was characterized by wide-angle XRD, energy-dispersive X-ray (EDX) spectroscopy, and elemental mapping by ultrahigh-resolution (UHR) TEM and X-ray photoelectron spectroscopy (XPS). N₂ adsorption-desorption isotherms showed BET surface areas of 389 and 385 m² g⁻¹ with an average pore size of about 3.2 nm. The mesoporosity of these core-shell materials is due to self-aggregation of tiny spherical nanocrystals of about 15–20 nm in size. These Al₂O₃@Fe₂O₃ core-shell nanoparticles act as a Fenton catalyst in the presence of hydrogen peroxide, and showed high catalytic activity for the conversion of cyclohexanone to adipic acid in a one-step reaction in water as a green reaction medium.

Results and Discussion

Characterization of Al₂O₃@Fe₂O₃ core-shell nanoparticles:

Small-angle powder XRD (PXRD) patterns of mesoporous γ -Al₂O₃ and Al₂O₃@Fe₂O₃-2 are shown in Figure 1. One broad peak signifying the average particle center-to-particle center correlation length is observed for both samples.^[19] The increase in this interparticle distance is related to the increase in particle size for the core-shell nanoparticles (see

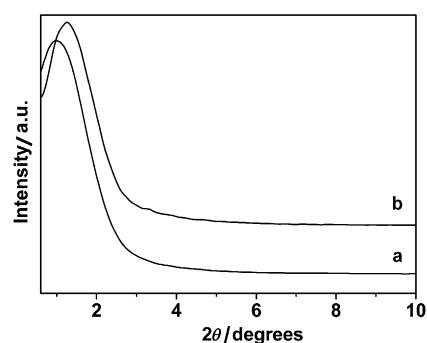


Figure 1. Small-angle XRD patterns of a) mesoporous γ -Al₂O₃ and b) Al₂O₃@Fe₂O₃-2 core-shell nanoparticles.

FESEM analysis below). The wide-angle XRD pattern of the Al₂O₃ nanoparticles (Figure 2a) suggested the presence of highly crystalline γ -Al₂O₃. Crystalline planes correspond-

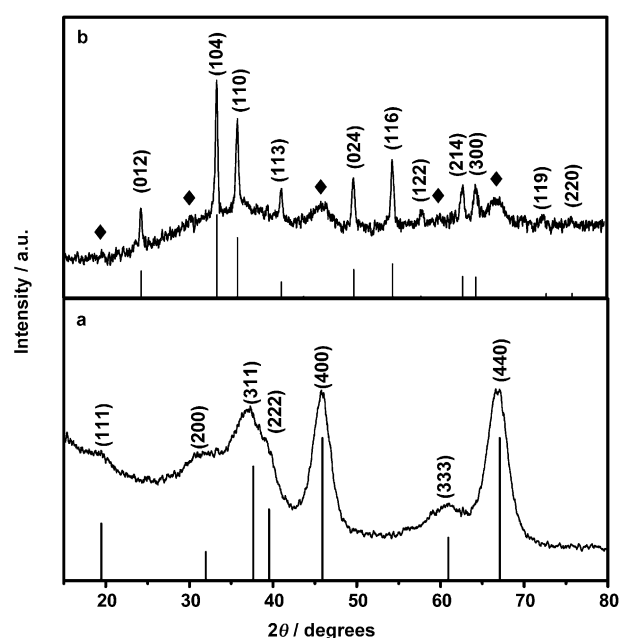


Figure 2. Wide-angle XRD patterns of a) mesoporous γ -Al₂O₃ and b) Al₂O₃@Fe₂O₃-2 core-shell nanoparticles. The planes are indexed in both cases and lines show the JCPDS data.

ing to the peaks for γ -Al₂O₃ were indexed. The calcined sample shows major peaks at 2θ values of 19.45, 31.93, 37.60, 39.49, 45.86, 60.89, and 67.03°, which correspond to γ -Al₂O₃ (111), (200), (311), (222), (400), (511), and (440) crystal planes, respectively (JCPDS PDF No. 10-0425).^[20]

All of the peaks are well indexed to a pure face-centered cubic structure of Al₂O₃ with an *Fd3m* space group and lattice parameter $a=7.9$. Thus, these powder XRD results revealed that we have synthesized highly stable and crystalline γ -Al₂O₃ spherical nanomaterials by using sodium salicylate as template. The crystallinity, phase, and the purity of the samples after α -Fe₂O₃ coating were determined by PXRD.

The wide-angle XRD pattern of the $\text{Al}_2\text{O}_3@\text{Fe}_2\text{O}_3$ -2 nanoparticles is shown in Figure 2b. Peaks for both $\gamma\text{-Al}_2\text{O}_3$ and $\alpha\text{-Fe}_2\text{O}_3$ are present. Peaks for $\gamma\text{-Al}_2\text{O}_3$ are marked with diamonds, and peaks for $\alpha\text{-Fe}_2\text{O}_3$ are indexed. The core-shell $\text{Al}_2\text{O}_3@\text{Fe}_2\text{O}_3$ nanoparticles show major peaks at 2θ values of 24.26, 33.33, 35.78, 41.05, 49.7, 54.36, 57.71, 62.74, 64.3, 72.4, and 75.83°, which correspond to $\alpha\text{-Fe}_2\text{O}_3$ (012), (104), (110), (113), (024), (116), (122), (214), (300), (119), and (220) crystal planes, respectively (JCPDS PDF No. 84-0308).^[21] All of the peaks are well indexed to a pure rhombohedral structure of Fe_2O_3 with an $R\bar{3}c$ space group and lattice parameters $a=5.01$, $c=13.6$. Thus, these powder XRD results revealed that we have synthesized highly stable and phase-pure crystalline $\text{Al}_2\text{O}_3@\text{Fe}_2\text{O}_3$ core-shell spherical nanomaterials.

Nanostructure analysis: TEM images of a representative self-assembled mesoporous $\text{Al}_2\text{O}_3@\text{Fe}_2\text{O}_3$ -2 core-shell nanoparticle are shown in Figure 3. As shown in Figure 3a, 15–

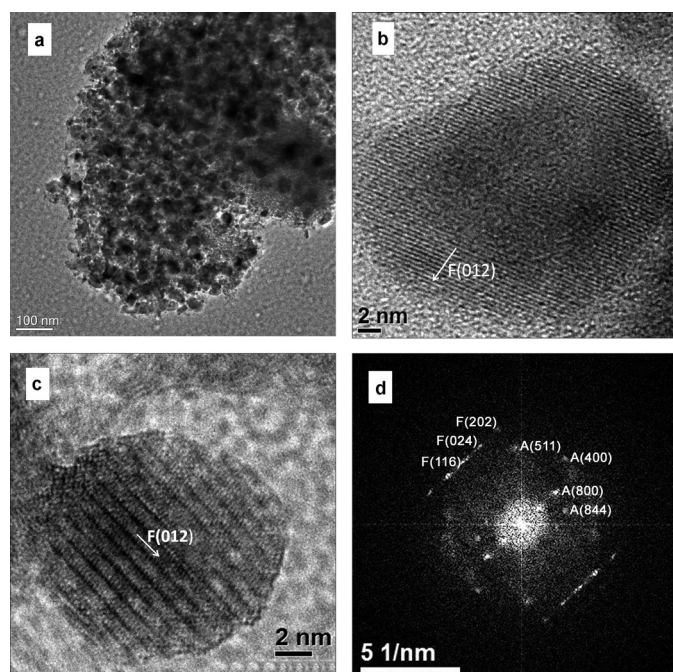


Figure 3. TEM images of a) self-assembled $\text{Al}_2\text{O}_3@\text{Fe}_2\text{O}_3$ -2 core-shell nanoparticles and b),c) single particles. In b) a peripheral $\alpha\text{-Fe}_2\text{O}_3$ layer and (012) lattice fringes are clearly seen. The FFT pattern of c) is shown in d). The spots are indexed to $\gamma\text{-Al}_2\text{O}_3$ (A) and $\alpha\text{-Fe}_2\text{O}_3$ (F).

20 nm spherical particles are self-assembled to form interparticle porosity and pores of about 3–6 nm in size (white spots), which are observed throughout the image (Figure 3a) for this sample. Furthermore, individual nanoparticles (Figure 3b and c) are seen clearly. In the UHRTEM image of a core-shell particle (Figure 3b), the peripheral $\alpha\text{-Fe}_2\text{O}_3$ shell is clearly seen with its (012) crystal plane. Lattice fringes corresponding to the crystalline phase are also quite clear in Figure 3c. The average thickness of the $\alpha\text{-Fe}_2\text{O}_3$ shell is about 5.0 nm according to the difference in contrast between

the core and shell regions. The fast Fourier transformation (FFT) of Figure 3c (Figure 3d) for this nanoparticle shows that it consists of $\gamma\text{-Al}_2\text{O}_3$ and $\alpha\text{-Fe}_2\text{O}_3$ and, in accordance with the synthetic procedure, these two metal oxides can co-exist in single nanoparticles only by forming a core-shell structure. The diffraction spots in the FFT are well indexed to those of the $\gamma\text{-Al}_2\text{O}_3$ and $\alpha\text{-Fe}_2\text{O}_3$ structures. These results suggested the formation of self-assembled mesoporous $\text{Al}_2\text{O}_3@\text{Fe}_2\text{O}_3$ -2 core-shell spherical nanoparticles with well-defined nanostructure. To better understand the core-shell structure, we recorded a dark-field STEM image (Figure 4a)

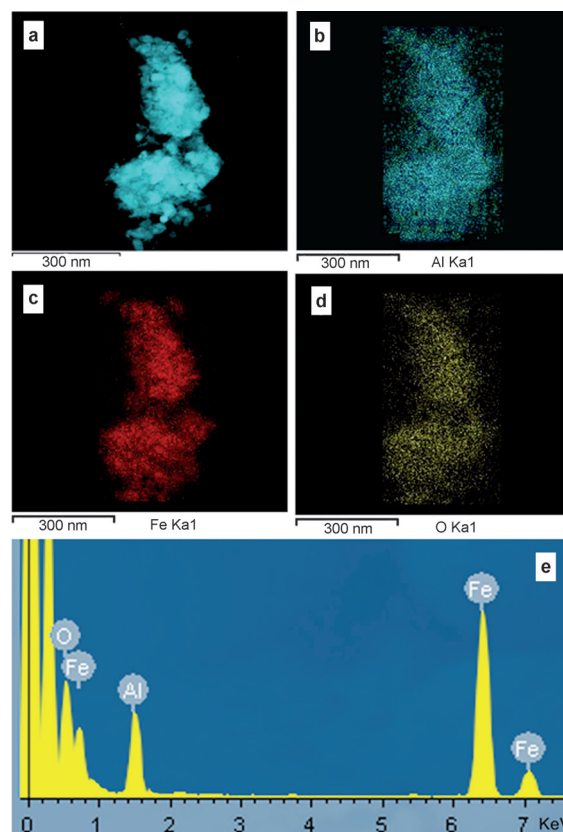


Figure 4. Dark-field STEM image of a) an $\text{Al}_2\text{O}_3@\text{Fe}_2\text{O}_3$ -2 core-shell nanoparticle and elemental mapping of b) Al, c) Fe, and d) O. The EDX spectrum of the core-shell $\text{Al}_2\text{O}_3@\text{Fe}_2\text{O}_3$ -2 nanoparticle is shown in e).

and performed elemental mapping. The EDX spectrum and elemental mapping of the core-shell $\text{Al}_2\text{O}_3@\text{Fe}_2\text{O}_3$ -2 nanoparticles are shown Figure 4. Elemental mapping for Al, Fe, and O is shown in Figure 4b, c, and d respectively, and all the elements are spread over the whole image with core-shell aggregation. These figures strongly suggest the presence of Al-rich particle with larger amount than Fe. This is most evident in Figure 4 when comparing the regions of the Al and Fe maps in which the large Al_2O_3 particles are encapsulated by thin Fe_2O_3 shells, as is seen in Figure 3b. Peaks for the elements Al, Fe, and O are clearly seen in the EDX spectrum.

The absence of peaks for other elements in the EDX spectrum indicates high purity of the $\text{Al}_2\text{O}_3@\text{Fe}_2\text{O}_3$ core–shell nanoparticles. The amounts of Fe, Al, and O in the sample of 21.7, 24.3, and 54 %, respectively, match well with the results from atomic adsorption spectroscopy (AAS) and XPS analysis. Elemental mapping revealed that the Al_2O_3 core is surrounded uniformly by Fe_2O_3 . Uniform and homogeneous particle size distributions are observed in the FESEM images of both samples (Figure 5). Figure 5a shows that the $\gamma\text{-Al}_2\text{O}_3$ particles are composed of tiny nanocrystals of 5–12 nm in size. The crystal edges of these particles are sharp due to the high synthesis temperature. In Figure 5b the particle size is increased and the material is composed of 15–20 nm tiny nanocrystals. The increase in particle size is taken due to attachment of the Fe_2O_3 layer at the periphery of Al_2O_3 .

We analyzed the surface composition of the $\text{Al}_2\text{O}_3@\text{Fe}_2\text{O}_3$ core–shell nanoparticles by XPS analysis, which provides important information about the surface electronic structure and the valence state of the elements present in a material. The XP spectra of the core–shell nanomaterials are shown in Figure 6. The binding energies obtained in the XPS analysis were corrected for specimen charging by referencing the O 1s line to 532 eV. The survey XPS spectra (Figure 6a and b) reveal that the core–shell nanomaterials are composed of Al, Fe, and O. Both $\text{Al}_2\text{O}_3@\text{Fe}_2\text{O}_3$ core–shell nanomaterials show major peaks at 74.9, 119.5, 532, 713.1, and 726.4 eV in the XP spectra, which correspond to Al 2p, Al 2s, O 1s, Fe 2p_{3/2}, and Fe 2p_{1/2}, respectively. The high-resolution Al spectra (Figure 6c and d) show two peaks at binding energies of 74.9 and 119.5 for Al 2p and Al 2s, respectively. This is characteristic of Al^{3+} in Al_2O_3 .^[22]

The Fe spectra also show two distinct peaks (Figure 6g and h) at binding energies of 713.1 eV for Fe 2p_{3/2} and 726.4 eV for Fe 2p_{1/2} with a satellite peak at 721.1 eV. This is characteristic of Fe^{3+} in Fe_2O_3 .^[23] Furthermore, on the basis of the quantification of Al, Fe, and O peaks by CasaXPS software, the average Al:Fe:O atomic ratios are about 0.60:0.27:1 and 0.45:0.4:1 for $\text{Al}_2\text{O}_3@\text{Fe}_2\text{O}_3$ -1 (Figure 6a) and $\text{Al}_2\text{O}_3@\text{Fe}_2\text{O}_3$ -2 (Figure 6b), respectively. With increasing the amount of Fe_2O_3 coating, the Al:Fe ratio determined by XPS analysis decrease. The corresponding powder XRD pattern provided further information on the crystallinity and phase for the core–shell nanomaterials, as shown in Figure 2.

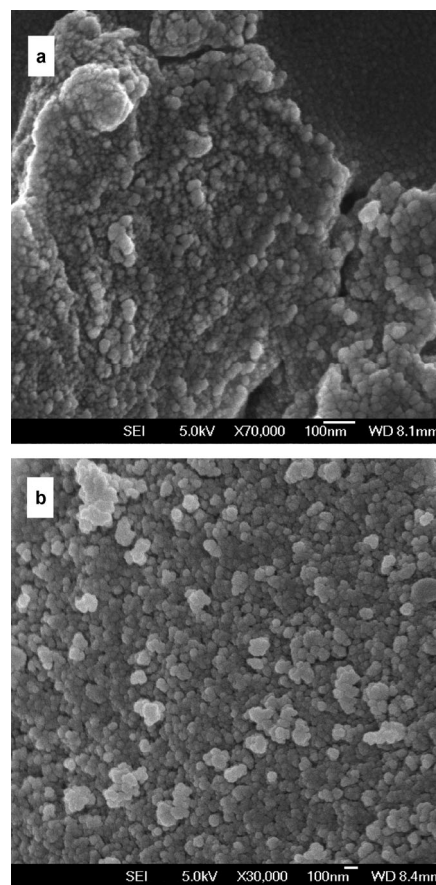


Figure 5. FESEM images of a) mesoporous $\gamma\text{-Al}_2\text{O}_3$ and b) $\text{Al}_2\text{O}_3@\text{Fe}_2\text{O}_3$ -2 core–shell nanoparticles.

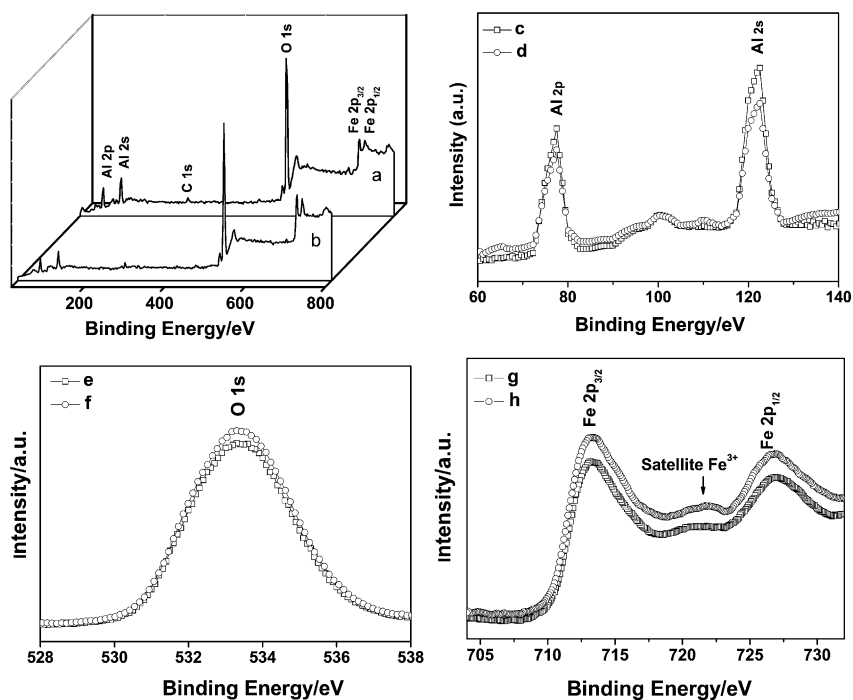
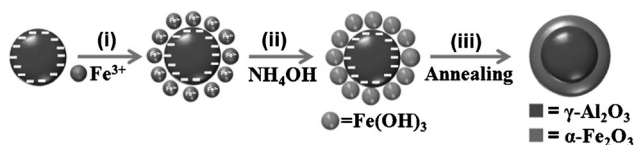


Figure 6. XP spectra of a) $\text{Al}_2\text{O}_3@\text{Fe}_2\text{O}_3$ -1 and b) $\text{Al}_2\text{O}_3@\text{Fe}_2\text{O}_3$ -2. High-resolution spectra of Al, O, and Fe are shown in c), e), g) and d), f), h) for $\text{Al}_2\text{O}_3@\text{Fe}_2\text{O}_3$ -1 and $\text{Al}_2\text{O}_3@\text{Fe}_2\text{O}_3$ -2, respectively.

Formation mechanism of Al₂O₃@Fe₂O₃ core-shell nanoparticles:

The formation of mesoporous self-assembled γ -Al₂O₃ by a sodium salicylate templated pathway was discussed in our previous work.^[11] The zeta potential ζ gives the overall net charge density of these metal oxides. For oxide materials at all pH values, there are large numbers of negative, neutral, or positive surface sites.^[24] Measurement of the zeta potential showed that the surface charge of the self-assembled γ -Al₂O₃ is positive in Millipore water and negative in Millipore water at pH 8 (Supporting Information Figure S1). The zeta potentials of this material are +6.97 and -32.7 mV in Millipore water and in Millipore water at pH 8, respectively. The synthetic route and formation mechanism for fabricating the mesoporous Al₂O₃@Fe₂O₃ core-shell heterostructure is shown in Scheme 1. Upon ultrasonication, the γ -Al₂O₃



Scheme 1. Synthetic route and formation mechanism of Al₂O₃@Fe₂O₃ mesoporous core-shell particles. i) The iron precursor is adsorbed on the surface of γ -Al₂O₃ at pH 8. ii) On adding ammonia to Fe(NO₃)₃ solution, Fe(OH)₃ is formed in basic solution. iii) Fe(OH)₃ decomposes and forms an α -Fe₂O₃ coating on annealing treatment, and these particles form the mesoporous structures.

particles are dispersed in the solution at pH 8. After addition of aqueous Fe(NO₃)₃ solution, the negatively charged surface adsorbed the positively charge Fe³⁺ ions by electrostatic interaction. On addition of aqueous ammonia the Fe³⁺ ions are converted to iron hydroxide at the periphery of γ -Al₂O₃. The hydroxide transformed into oxide on annealing. Due to the presence of the Fe₂O₃ layer at the periphery of Al₂O₃ the particle size is increased, as was seen in the HRTEM and FESEM images.

N₂ adsorption-desorption study on core-shell nanoparticles:

The N₂ adsorption-desorption isotherms of γ -Al₂O₃, Al₂O₃@Fe₂O₃-2, and Al₂O₃@Fe₂O₃-1 are shown in Figure 7 and the Supporting Information (Figure S2). They could be classified as type IV isotherms characteristic of mesoporous materials.^[25] In the relative pressure range of $P/P_0=0.01-0.60$, the adsorbed amount gradually increases for all of the samples, but above $P/P_0>0.6$ N₂ uptake becomes saturated. The BET surface areas for calcined samples of γ -Al₂O₃, Al₂O₃@Fe₂O₃-1, and Al₂O₃@Fe₂O₃-2 were 493, 389 and 385 m²g⁻¹, respectively. Their respective pore volumes were 0.36, 0.32, and 0.29 cm³g⁻¹. Pore size distributions of these samples, obtained by employing the BJH model (N₂ adsorption on silica as reference)^[11] suggested that γ -Al₂O₃ synthesized at 393 K has an average pore width of about 3.6 nm as opposed to about 3.2 nm for Al₂O₃@Fe₂O₃. Pore widths obtained from N₂ sorption analysis agree well with those obtained independently by TEM image analysis.

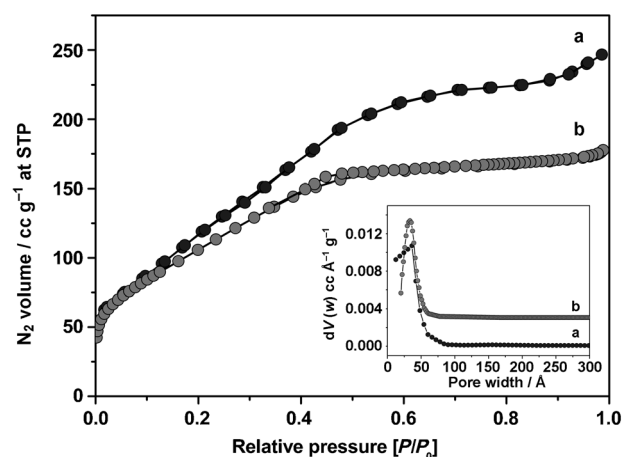


Figure 7. N₂ adsorption-desorption isotherms of a) mesoporous γ -Al₂O₃ and b) Al₂O₃@Fe₂O₃-2 core-shell nanoparticles. Pore size distributions obtained by using the BJH model are shown as insets.

UV/Vis spectroscopy and bandgap analysis:

UV/Vis spectroscopy is one of the most important analytical tools for characterizing the optical properties of nanocrystals. The diffuse-reflectance UV/Vis spectrum of calcined mesoporous γ -Al₂O₃ and Al₂O₃@Fe₂O₃-2 core-shell materials are shown in Figure 8. The γ -Al₂O₃ material shows an absorption band at

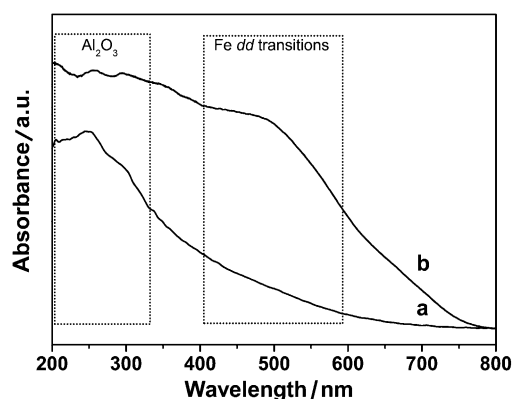


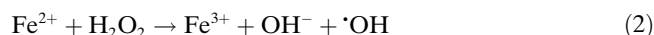
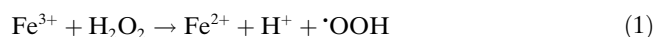
Figure 8. UV/Vis diffuse-reflectance spectra of a) mesoporous γ -Al₂O₃ and b) core-shell Al₂O₃@Fe₂O₃-2 (b).

247 nm, which corresponds to a bandgap energy of 3.43 eV (Supporting Information Figure S3). This bandgap energy is much lower than the direct bandgap of 6.31 eV for bulk γ -Al₂O₃.^[26] The Al₂O₃@Fe₂O₃-2 core-shell sample shows absorption bands at 255 and 497 nm, which correspond to a bandgap of 2.3 eV (Supporting Information Figure S3). The peak corresponding to alumina is observed at 255 nm, and that at 497 nm could be attributed to the d-d transition between ground and excited state of Fe³⁺ present in the core-shell framework.^[27]

Catalysis: Since 1900 Fenton's reagents have had an interesting and colorful story.^[28] They act as an oxidizing agents for the oxidation of a large variety of substrates. Fenton's

reagents have been extensively investigated and applied for the removal of organic, often toxic, pollutants from various wastewaters and soils.^[29]

We have used the newly synthesized iron-containing core–shell nanoparticles and H₂O₂ as a Fenton's reagent for the one-pot oxidation of cyclohexanone to an industrially important compound, namely, adipic acid. The catalytic performance of the Al₂O₃@Fe₂O₃-1 and Al₂O₃@Fe₂O₃-2 mesoporous core–shell nanoparticles was investigated in the oxidation of cyclohexanone in aqueous medium. The presence of a large amount of Fe³⁺ at the surface of the catalyst facilitates the production of hydroxyl radicals according to Equations (1) and (2).^[28]



The kinetic plot for the oxidation of cyclohexanone in aqueous medium is shown in Figure 9. Initially, the reaction increases in rate up to 6 h, after which it proceeds slowly. In-

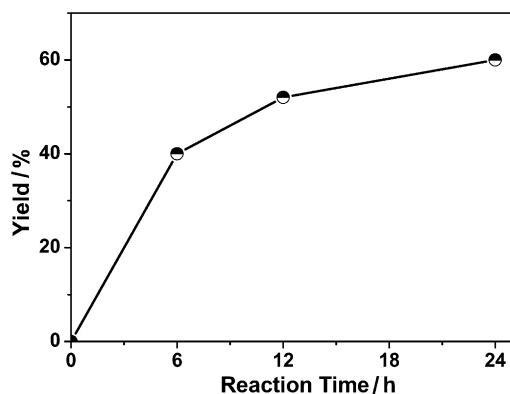


Figure 9. Reaction kinetics of the oxidation of cyclohexanone to adipic acid.

Initially Fe³⁺ activated the H₂O₂ and produced active hydroxyl radicals.^[28] The hydroxyl radical attacked the activated carbonyl carbon atom of cyclohexanone and converted it to caprolactone. The caprolactone was hydrolyzed under the reaction condition to produce 6-hydroxyhexanoic acid, which was further oxidized to adipic acid in the presence of H₂O₂. The complete balance reaction is shown in Equation (3).



Here C₆H₁₀O, C₆H₁₀O₄, C₆H₁₀O₂, and C₆H₁₀O₃ are cyclohexanone, adipic acid, caprolactone, and 6-hydroxyhexanoic acid, respectively. The course of the reactions was monitored by gas chromatographic analysis with *tert*-butanol as internal standard. The composition of the reaction at different time

interval is given in the Table S1 of the Supporting Information in detail. After 24 h, the reaction shows 69% conversion with respect to cyclohexanone. In this mixture the selectivities for adipic acid, caprolactone, and 6-hydroxyhexanoic acid were 86.0, 5.9, and 7.9%, respectively. A probable mechanistic pathway of this reaction is suggested in Figure S4 of the Supporting Information. Our experimental results suggested that the Al₂O₃@Fe₂O₃-1 and Al₂O₃@Fe₂O₃-2 core–shell nanoparticles showed excellent catalytic efficiency for the production of adipic acid. Only 3 wt% of catalyst with respect to cyclohexanone was employed to produce 55.4 and 60% adipic acid (yield of isolated product) in this reaction at 353 K. The same reaction was carried with bulk α-Fe₂O₃ as the catalyst to verify the role of the porous nanostructure. After the same reaction time, the yield of adipic acid was 24%. Bulk α-Fe₂O₃ gives lower conversion of adipic acid because it has much less surface area (47 m²g⁻¹) and pore volume (0.0932 ccg⁻¹). It shows very poor conversion, together with low turnover numbers (TON) and frequencies (TOF; Table 1). All of the observed TONs and

Table 1. Physical properties and catalytic activities of core–shell nanomaterials

Sample	BET surface area [m ² g ⁻¹]	Al:Fe:O ratio from XPS	TON	TOF [h ⁻¹]
γ-Al ₂ O ₃	497	–	–	–
Al ₂ O ₃ @Fe ₂ O ₃ -1	489	0.61:0.27:1	71.0	2.90
Al ₂ O ₃ @Fe ₂ O ₃ -2	485	0.45:0.4:1	51.7	2.15
α-Fe ₂ O ₃	47	–	6.3	0.26

TOFs reported in Table 1 are relatively low, because only the surface Fe center takes part in the reaction. Fe present inside the core–shell structure does not take part in the reaction. However, when calculating the Fe loading, we took account of all Fe atoms present in the core–shell catalyst (both surface atoms and those located close to the core). Thus, a considerably higher Fe loading decreases the TON and TOF. The catalytic reaction was repeated for five cycles, and there was no significant loss of catalytic efficiency. The recycling efficiency is shown in Figure S5 of the Supporting Information. After the five cycles the catalysts have same structure according to wide-angle XRD studies (Supporting Information Figure S6). Thus, our mesoporous core–shell Al₂O₃@Fe₂O₃ nanoparticles have very good catalytic efficiency due to the porous nanostructure, which facilitates the interaction between the reactant molecules and the active sites of the catalyst.

Conclusion

We have prepared mesoporous, phase-pure, crystalline Al₂O₃@Fe₂O₃ core–shell nanoparticles by a new synthetic strategy. The negative charge on the surface of γ-Al₂O₃ helps the formation of the core–shell nanostructure. The core–shell structure was well established by wide-angle

XRD, UHRTEM with elemental mapping, and HRTEM images with FFT pattern. The N_2 adsorption–desorption isotherm showed a BET surface area of $Al_2O_3@Fe_2O_3$ of $385\text{ m}^2\text{ g}^{-1}$ and an average pore size of about 3.2 nm, and the mesoporosity of this core–shell material is due to self-aggregation of tiny spherical nanocrystals of about 15–20 nm in size. These core–shell nanoparticles act as a heterogeneous Fenton nanocatalyst in the presence of H_2O_2 and show high catalytic activity for the conversion of cyclohexanone to adipic acid in water in one step.

Experimental Section

Preparation of $\gamma\text{-}Al_2O_3$: Self-assembled $\gamma\text{-}Al_2O_3$ nanomaterials were synthesized by employing our previous procedure.^[24] In this typical synthesis, ammonium chloride (2.0 g, 37.4 mmol, E. Merck, 98.9% GR) was added to 20 mL of an aqueous solution of sodium salicylate (1.6 g, 10 mmol, E. Merck, 99.5%). The solution was stirred for 15 min. Then 4 mL of 25% aqueous ammonia solution was added and the mixture stirred again for 30 min. Then anhydrous $AlCl_3$ (1.33 g, 10 mmol, E. Merck) was dissolved in 5.0 g distilled water, and this solution was slowly added to the above solution. The pH of the solution was adjusted to about 10 by addition of ammonia solution and the resulting mixture stirred for 3 h. Then the mixture was transferred into a Teflon-lined stainless steel autoclave and hydrothermally treated at 393 K for 24 h. The light yellow solid was collected by filtration, washed with water, dried at room temperature under vacuum, and designated MA-1. The as-synthesized sample was calcined at 773 K for 6 h to remove the template molecules and thus generate mesoporosity, and these nanoparticles were used in preparation of the $Al_2O_3@Fe_2O_3$ core–shell nanoparticles.

Preparation of $Al_2O_3@Fe_2O_3$ core–shell nanoparticles: $\gamma\text{-}Al_2O_3$ (0.5 g, BET surface area $495\text{ m}^2\text{ g}^{-1}$) was dispersed in 100 mL of distilled water and sonicated for 2 h. After sonication, the solution was stirred with a magnetic stirrer at 1200 rpm for 15 min. During this time ammonium hydroxide was added to adjust the pH (ca. 8) of the solution. $Fe(NO_3)_3 \cdot 9H_2O$ (0.51 g, 1.25 mmol, E. Merck) was dissolved in 5 mL of water and added slowly to the above solution. The solution was stirred for 30 min. Then 3 mL of aqueous ammonia was added and the solution became deep brown in color. After 30 min of stirring, the solution was centrifuged and washed with water. In another synthesis $Fe(NO_3)_3 \cdot 9H_2O$ (1.01 g, 2.5 mmol, E. Merck) was used under the same reaction conditions. Both of the brown solids were dried thoroughly at room temperature and annealed at 873 K for 6 h. These materials were termed $Al_2O_3@Fe_2O_3$ -1 and $Al_2O_3@Fe_2O_3$ -2, respectively.

Zeta-potential measurements on $\gamma\text{-}Al_2O_3$ nanoparticles: For zeta-potential measurements, 0.010 g of $\gamma\text{-}Al_2O_3$ was dispersed in 50 mL of Millipore water and 50 mL Millipore water with pH 8. Ammonium hydroxide was used for pH adjustment. The solutions were sonicated for 2 h prior to measurement, and 2 mL of the solutions was used for analysis. Disposable polystyrene cuvettes were used for the measurement.

Catalysis procedure: The oxidation of cyclohexanone with mesoporous $Al_2O_3@Fe_2O_3$ -2 core–shell nanoparticles was carried out in a 50 mL two-necked round-bottom flask fitted with a water condenser and placed in an oil bath at 353 K with vigorous stirring. In a typical reaction procedure, cyclohexanone (0.5 g, 5 mmol) was suspended in 5 mL of double-distilled water, and 0.015 g of preheated catalyst and 1 g H_2O_2 (E. Merck, 30%) were added. The reaction was carried out for 24 h with *tert*-butanol as internal standard, which allowed convenient sampling and full quantitative analysis including side products and a mass balance. At selected time intervals the products were collected from the reaction mixtures and analyzed by capillary gas chromatography (Agilent 4890D, FID). Products were identified from known standards. To determine the yield of isolated product, the mixture was filtered under hot conditions to remove the catalyst from the reaction mixture. The filtrate was extracted

with chloroform to separate unconverted reactant from the filtrate, the aqueous fraction was concentrated in rotary evaporator, and solid adipic acid was collected. The product was characterized by 1H and ^{13}C NMR and FTIR spectroscopy (Supporting Information Figures S7, S8, and S9, respectively). The separated catalyst was washed with water and dried at room temperature under high vacuum before conducting the recycling experiments. Catalyst recycling was carried out for five times. Spectral characterization of adipic acid: 1H NMR (500 MHz, $[D_6]DMSO$) δ = 11.96 (s, 2H, CO_2H), 2.18 (m, 4H; $\alpha\text{-}CH_2$), 1.47 ppm (m, 4H; $\beta\text{-}CH_2$); ^{13}C NMR (500 MHz, $[D_6]DMSO$) δ = 174.89 (CO_2H), 33.91 ($\alpha\text{-}CH_2$), 24.57 ppm ($\beta\text{-}CH_2$); IR (KBr): $\tilde{\nu}$ = 3415 ($\nu(OH)$, H_2O), 2953 ($\nu(OH)$), 2648 ($\nu(CH)$), 1703 ($\nu(C=O)$), 1405 (s (CH)), 1282 ($\nu(CO)$), 1058 cm^{-1} ($\nu(CC)$), m.p. 148–151°C. Note that we did not check amount of oxygen evolved due to decomposition of H_2O_2 because the reactions proceeded smoothly under atmospheric pressure (open system), and any attempt to use a gas burette to measure oxygen evolution would make the system closed and thus affect the product yield.

Hot filtration test: To confirm the heterogeneous nature of the catalyst and catalytic activity bound to the solid phase, a hot filtration test was performed.^[30] The $Al_2O_3@Fe_2O_3$ -2 mesoporous core–shell catalyst (0.015 g), cyclohexanone (0.5 g, 5 mmol), and H_2O_2 (1 g, 30%) in 5 mL of H_2O were heated to reflux at 353 K for 8 h. The catalyst was filtered off from the hot reaction mixture after 8 h, at which time the reaction had reached 46% conversion (GC and 1H NMR). The reaction was continued with the filtrate for another 6 h at the same reaction temperature. No increase in the amount of product beyond 46% was observed. Iron was also not detected (AAS) in the liquid phase after the completion of the reaction for 8 h, and the filtrate remained completely colorless. On the basis of these results we concluded that iron is not leached from $Al_2O_3@Fe_2O_3$ and that the observed catalysis is heterogeneous in nature.

Characterization techniques: Powder X-ray diffraction patterns of the samples were recorded on a Bruker D-8 Advance diffractometer operated at 40 kV and 40 mA with $Cu_{K\alpha}$ radiation ($\lambda = 0.15406\text{ nm}$). UHRTEM images were recorded in a JEOL 2010F TEM operated at 200 kV. A JEOL JEM 6700F field-emission (FE) scanning electron microscope was used for the determination of particle morphology. Nitrogen sorption isotherms were obtained using a Beckman Coulter surface area analyzer at 77 K. Prior to the measurement, the samples were degassed at 393 K for 3 h. UV/Vis diffuse-reflectance spectra were recorded on a Shimadzu UV 2401PC with an integrating-sphere attachment. $BaSO_4$ was used as background standard. Iron content in the $Al_2O_3@Fe_2O_3$ core–shell nanoparticles was estimated by using a Shimadzu AA-6300 atomic absorption spectrometer (AAS) fitted with a double-beam monochromator. Zeta potentials of the materials were recorded by Malvern particle size analyzer model no. ZEN 3690 Zetasizer nano ZS 90. X-ray photoluminescence spectroscopy (XPS) was performed on a Omicron nanotech operated at 15 kV and 20 mA with a monochromatic $Al_{K\alpha}$ X-ray source. The reaction mixtures of the catalytic reactions were analyzed by capillary gas chromatography (Agilent Model 4890D gas chromatograph equipped with a flame ionization detector).

Acknowledgements

A.K.P. and A.D. thank CSIR, New Delhi for their senior research fellowships. A.B. wishes to thank DST New Delhi for providing instrumental facility through DST Unit on Nanoscience.

- [1] a) S. Wei, Q. Wang, J. Zhu, Sun, H. L. Lin, Z. Guo, *Nanoscale* **2011**, 3, 4474–4502; b) M. K. Carpenter, T. E. Moylan, R. S. Kukreja, M. H. Atwan, M. M. Tessema, *J. Am. Chem. Soc.* **2012**, 134, 8535–8542; c) M. Shao, F. Ning, Y. Zhao, J. Zhao, M. Wei, D. G. Evans, X. Duan, *Chem. Mater.* **2012**, 24, 1192–1197; d) D. Rosario-Amorin, M. Gaboyard, R. Clerac, L. Vellutini, S. Nlate, K. Heuze, *Chem. Eur. J.* **2012**, 18, 3305–3315.

- [2] a) P. Reiss, M. Protiere, L. Li, *Small* **2009**, *5*, 154; b) Z. Khani, M. L. Taillades-Jacquín, G. Taillades, D. J. Jones, M. Marrony, J. Rozie're, *Chem. Mater.* **2010**, *22*, 1119–1125; c) R. Hudson, A. Riviere, C. M. Cirtiu, K. L. Luska, A. Moores, *Chem. Commun.* **2012**, *48*, 3360–3362; d) M. Nowotny, L. N. Pedersen, U. Hanefeld, T. Maschmeyer, *Chem. Eur. J.* **2002**, *8*, 3724–3731.
- [3] a) T. Sen, A. Sebastianelli, I. J. Bruce, *J. Am. Chem. Soc.* **2006**, *128*, 7130–7131; b) Y. Deng, C. Deng, D. Qi, C. Liu, J. Liu, X. Zhang, D. Zhao, *Adv. Mater.* **2009**, *21*, 1377–1382.
- [4] L. Li, Y. Feng, Y. Li, W. Zhao, J. Shi, *Angew. Chem.* **2009**, *121*, 6002–6006; *Angew. Chem. Int. Ed.* **2009**, *48*, 5888–5892.
- [5] a) J. Kim, Y. Piao, T. Hyeon, *Chem. Soc. Rev.* **2009**, *38*, 372–390; b) J. A. Liu, W. B. Bu, S. J. Zhang, F. Chen, H. Y. Xing, L. M. Pan, L. P. Zhou, W. J. Peng, J. L. Shi, *Chem. Eur. J.* **2012**, *18*, 2335–2341.
- [6] a) J. Li, H. Zeng, S. H. Sun, J. P. Liu, Z. L. Wang, *J. Phys. Chem. B* **2004**, *108*, 14005–14008.
- [7] a) N. S. Froemming, G. Henkelman, *J. Chem. Phys.* **2009**, *131*, 234103; b) A. P. Majewski, A. Schallon, V. Jerome, R. Freitag, A. H. E. Mueller, H. Schmalz, *Biomacromolecules* **2012**, *13*, 857–866.
- [8] a) Y. Piao, A. Burns, J. Kim, U. Wiesner, T. Hyeon, *Adv. Funct. Mater.* **2008**, *18*, 3745–3758; b) M. Liong, S. Angelos, E. Choi, K. Patel, J. F. Stoddart, J. I. Zink, *J. Mater. Chem.* **2009**, *19*, 6251–6257.
- [9] M. B. Zaman, D. Bardelang, M. Prakesch, D. M. Leek, J.-V. Naubron, G. Chan, X. Wu, J. A. Ripmeester, C. I. Ratcliffe, K. Yu, *ACS Appl. Mater. Interfaces* **2012**, *4*, 1178–1181.
- [10] a) C. N. R. Rao, S. R. C. Vivekchand, K. Biswas, A. Govindaraj, *Dalton Trans.* **2007**, 3728–3749; b) G. Chen, S. Desinan, R. Nechache, R. Rosei, F. Rosei, D. Ma, *Chem. Commun.* **2011**, *47*, 6308–6310; c) H. Zhang, M. Jin, J. Wang, W. Li, P. H. C. Camargo, M. J. Kim, D. Yang, Z. Xie, Y. Xia, *J. Am. Chem. Soc.* **2011**, *133*, 6078–6089; d) L. Wang, Y. Nemoto, Y. Yamauchi, *J. Am. Chem. Soc.* **2011**, *133*, 9674–9677; e) M. R. Jones, K. D. Osberg, R. J. Macfarlane, M. R. Langille, C. A. Mirkin, *Chem. Rev.* **2011**, *111*, 3736–3827; f) R. Huang, Y.-H. Wen, Z.-Z. Zhu, S.-G. Sun, *J. Phys. Chem. C* **2012**, *116*, 11837–11841.
- [11] A. K. Patra, A. Dutta, A. Bhaumik, *J. Hazard. Mater.* **2012**, *201*, 170–177.
- [12] K. Sato, M. Aoki, R. Noyori, *Science* **1998**, *281*, 1646–1647.
- [13] A. Castellan, J. C. J. Bart, S. Cavallaro, *Catal. Today* **1991**, *9*, 237–254.
- [14] Z. Bohström, I. Rico-Lattes, K. Holmberg, *Green Chem.* **2010**, *12*, 1861–1869.
- [15] a) Y. Deng, Z. Ma, K. Wang, J. Chen, *Green Chem.* **1999**, *1*, 275–276; b) M. Waki, N. Mizoshita, Y. Maegawa, T. Hasegawa, T. Tani, T. Shimada, S. Inagaki, *Chem. Eur. J.* **2012**, *18*, 1992–1998.
- [16] X. She, H. M. Brown, X. Zhang, B. K. Ahring, Y. Wang, *ChemSusChem* **2011**, *4*, 1071–1073.
- [17] M. Dugal, G. Sankar, R. Raja, J. M. Thomas, *Angew. Chem.* **2000**, *112*, 2399–2402; *Angew. Chem. Int. Ed.* **2000**, *39*, 2310–2313.
- [18] A. Dutta, M. Pramanik, A. K. Patra, M. Nandi, H. Uyama, A. Bhaumik, *Chem. Commun.* **2012**, *48*, 6738–6740.
- [19] A. K. Patra, S. K. Das, A. Bhaumik, *J. Mater. Chem.* **2011**, *21*, 3925–3930.
- [20] H. Li, L. Zhang, H. Dai, H. He, *Inorg. Chem.* **2009**, *48*, 4421–4434.
- [21] X. Li, W. Wei, S. Wang, L. Kuai, B. Geng, *Nanoscale* **2011**, *3*, 718–724.
- [22] a) M. J. Capitan, M. A. Centeno, P. Malet, I. Carrizosa, J. A. Odriozola, *J. Phys. Chem.* **1995**, *99*, 4655–4660; b) L. Olsson, E. Fridell, *J. Catal.* **2002**, *210*, 340–353.
- [23] a) Y. Ni, X. Ge, Z. Zhang, Q. Ye, *Chem. Mater.* **2002**, *14*, 1048–1052; b) X. Hu, J. C. Yu, J. Gong, Q. Li, G. Li, *Adv. Mater.* **2007**, *19*, 2324–2329; c) T. Droubay, S. A. Chambers, *Phys. Rev. B* **2001**, *64*, 205414.
- [24] a) F. Q. Tang, T. Uchikoshi, K. Ozawa, Y. Sakka, *Mater. Res. Bull.* **2002**, *37*, 653–660; b) L. Yang, Q. Zhu, S. Guo, B. Qian, C. Xia, H. Huang, *Chem. Eur. J.* **2010**, *16*, 1638–1645.
- [25] a) M. Nandi, M. Islam, P. Mondal, A. Bhaumik, *Eur. J. Inorg. Chem.* **2011**, 221–227; b) S. Dutta, A. K. Patra, S. De, A. Bhaumik, B. Saha, *ACS Appl. Mater. Interfaces* **2012**, *4*, 1560; c) A. K. Patra, A. Dutta, A. Bhaumik, *ACS Appl. Mater. Interfaces* **2012**, *4*, 5022–5028; d) A. Dutta, J. Mondal, A. K. Patra, A. Bhaumik, *Chem. Eur. J.* **2012**, *18*, 13372–13378.
- [26] W. Y. Ching, L. Ouyang, P. Rulis, H. Yao, *Phys. Rev. B* **2008**, *78*, 014106.
- [27] D. Y. Inamdar, A. K. Pathak, I. Dubenko, N. Ali, S. Mahamuni, *J. Phys. Chem. C* **2011**, *115*, 23671–23676.
- [28] G. Z. Chen, *Angew. Chem.* **2010**, *122*, 5541–5543; *Angew. Chem. Int. Ed.* **2010**, *49*, 5413–5415.
- [29] a) J. H. Ma, W. J. Song, C. C. Chen, W. H. Ma, J. C. Zhao, Y. L. Tang, *Environ. Sci. Technol.* **2005**, *39*, 5810–5815; b) A. Noorjahan, V. D. Kumari, A. Subrahmanyam, L. Panda, *Appl. Catal. B* **2005**, *57*, 291–298; c) B. Zhao, G. Mele, I. Pio, J. Li, L. Palmisano, G. J. Vasapollo, *J. Hazard. Mater.* **2010**, *176*, 569–574; d) L. Liu, G. Zhang, L. Wang, T. Huang, L. Qin, *Ind. Eng. Chem. Res.* **2011**, *50*, 7219–7227; e) X. Zhou, J. Lan, G. Liu, K. Deng, Y. Yang, G. Nie, J. Yu, L. Zhi, *Angew. Chem.* **2012**, *124*, 182–186; *Angew. Chem. Int. Ed.* **2012**, *51*, 178–182.
- [30] R. Sheldon, M. Wallau, I. W. C. E. Arends, U. Schuchardt, *Acc. Chem. Res.* **1998**, *31*, 485–493.

Received: April 19, 2013
Published online: August 12, 2013